Manuscript to AIChE Journal, 11/2020

Alternating Magnetic Field Enhances Photocatalytic CO_2 Reduction

Xianhe Li[†], Ke Wang[†], Quanhao Shen[†], Boya Min[‡], Dengwei Jing[‡,], Maochang Liu[‡,#], Naixu Li[†,§,*]*

[†]School of Chemistry and Chemical Engineering, Southeast University, Nanjing 211189, P. R. China

[‡]International Research Center for Renewable Energy, State Key Laboratory of Multiphase Flow in Power Engineering, Xi'an Jiaotong University, Xi'an, Shaanxi 710049, P. R. China

[§]Jiangsu Key Laboratory for Biomass Energy and Material, Nanjing 210042, P. R. China

[#]Suzhou Academy of Xi'an Jiaotong University, Suzhou, Jiangsu 215123, P. R. China

*To whom correspondence should be addressed.

Email: dwjing@mail.xjtu.edu.cn (D. J.) and naixuli@seu.edu.cn (N. L.)

ABSTRACT

Solar CO_2 reduction via photocatalysis enables sustainable carbon-cycle utilization, yet a challenge to date because of the relatively low conversion efficiency. Herein, we demonstrate that this photocatalytic process could be significantly improved by coupling an alternating magnetic field (AMF). Using NiO/TiO_2 as a model photocatalyst, CO_2 could be converted into CH_4 in the presence of H_2O vapor. Integrating with AMF, the conversion of CO_2 to CH_4 increased by 213%. The enhanced photocatalysis process by AMF coupling can not only increase the carrier density by inhibiting the combination of photogenerated electron-hole pairs, but also improve the oxidation ability of the catalyst under simulated sunlight, and promote the conversion of H_2O to O_2. Our investigation also elucidates that the Ni species act as the adsorption/activation sites of CO_2 to promote the reduction of CO_2 to CH_4. This work opens a new research door in solar CO_2 reduction by integrating AMF into photocatalysis.

KEYWORDS: alternating magnetic field, CO_2 reduction, photocatalysis, solar energy, nanoparticles

1. INTRODUCTION

Photocatalytic CO_2 reduction by using solar energy is one of the most promising solutions to global warming and environmental issues.[1-3] Several methods, including photocatalysis, electrocatalysis, photoelectrocatalysis, and hydrogenation, have been investigated for the CO_2 reduction.[4-5] The main challenges lie in improving CO_2 conversion, increasing the product selectivity, and enhancing solar energy efficiency.[6-7] In 1972, Fujishima and Honda discovered water splitting on the TiO_2 electrode, which ushered in a new era of semiconductor-based non-homogeneous photocatalysis.[8] Later, in 1979, Inoue and co-workers reported the phenomena of photocatalytic CO_2 conversion into formic acid, formaldehyde, and methyl alcohol, which prompted scientists to have the research field extensively proexplored.[9] Generally, accelerating the migration and suppressing the recombination of photogenerated carriers are the mainly recommended strategies to improve the efficiency of CO_2 conversion. Gao and co-workers showed that a porphyrin-involved metal-organic framework (MOF), PCN-222, effectively inhibited the detrimental, radiative electron-hole recombination to enhance the photocatalytic conversion of CO_2.[10] Although these researches have made great progress, the photocatalytic CO_2 reduction is mainly focused on improving the performance of traditional semiconductor materials by modifying and optimizing, as well as designing and synthesizing new light-responsive materials.

Recently, the external field coupling method has also been widely used in the photocatalytic reaction process. In 2020, Isari and co-workers found that N-Cu co-doped TiO2@CNTs had a

superb catalytic capability for decomposition of non-biodegradable compounds and pharmaceutical effluents under visible light and ultrasonic irradiation.[11] Haile and co-workers proposed to the solar energy concentration method to thermochemically reduce CO_2 with H_2O to CO and H_2.[12] Although these works show that the photocatalytic efficiency is improving, it still falls short of expectations. Applying the magnetic field into photocatalysis has attracted intense attention because of the possibility of electron behavior manipulation by magnetic field. Xie and co-workers reported the significantly improved photocatalytic activity over an as-synthesized $Bi_2O_3/SrFe_{12}O_{19}$ magnetic photocatalyst.[13] The improvement attributes to magnetic-field-induced shunt effect for photoexcited electrons. Li and co-workers optimized the photocatalytic performance promoted under the magnetic field by increasing carriers from α-Fe_2O_3 to rGO.[14] On one hand, constructing a direct magnetic field into the reaction system could inhibit the recombination of the electron-hole pairs or improve the efficiency of spin polarization of the active catalyst surface.[14-16] On the other hand, a range of typical magnetic catalysts with a built-in magnetic field exhibits excellent photocatalytic performance.[13, 17] So far, researchers have paid much attention to free radicals, which are usually unpaired electrons of atoms or molecules and rather reactive. The magnetic effect could affect the radical-pair recombination, which is governed by the spin-exchange interaction between the two unpaired electrons located on the radicals.[18-19] By the time a pair of radicals occur on two different molecules, we call it either the singlet or the triplet state, which can appear with a chemical process such as bond break or photoinduced electron transfer.[20-21] In the field of spin chemistry, spin multiplicity occurred in the inner-molecular is defined as singlet-triplet interconversion. The spin-conserving nature and

singlet-triplet interconversion in radical pairs are sensitive to external magnetic field. For example, the magnetic field leads to different selectivity toward certain products while the recombination of singlet and triplet state of molecular direct to different reaction pathways.[22] The activity of photocatalytic CO_2 reduction is usually enhanced by magnetic field which suppresses the recombination of electron-hole pairs and affects the free radicals of atoms or molecules with an unpaired electron.

Despite these successful demonstrations, few reports emphasize the effect of an AMF on photocatalytic CO_2 reduction. In this study, a traditional NiO/TiO_2 catalyst was prepared using a one-step hydrothermal method. The obtained NiO/TiO_2 photocatalyst was applied to photocatalytic conversion of CO_2-H_2O mixture by using a coupled optical-magnetic system. The efficiency of photocatalytic CO_2 reduction was significantly enhanced after applying the alternating magnetic field (AMF), and the mechanism of improvement was also discussed. To the best of our knowledge, it should be the first report that the role of AMF in photocatalytic CO_2 reduction has been systematically investigated.

2. EXPERIMENTAL SECTION

2.1. Materials. Titanium dioxide (Degussa P25) and nickel (Ni) were purchased from Sinopharm Chemical Reagent Co., Ltd. All reagents and solvents above were analytical grade and were used as received without further purification. Carbon dioxide in nitrogen gas (1.0% CO_2, 99.0% N_2) was purchased from Nanjing Shangyuan Industrial Gas Plant. Deionized water was used throughout the research.

2.2. Synthesis. The 0.1 wt % NiO/TiO_2 composite was successfully prepared by a facile one-step hydrothermal method. Typically, after dispersing 0.5 g of titanium dioxide (Degussa P25) and 0.5 mg of nickel powder (particle size: 20-100 nm), in 50 mL deionized water with the help of ultrasonication for 15 min, the uniform suspension was gray-white. The above solution was heated at 423 K for ten hours in a Teflon-lined stainless-steel autoclave. Next, a light yellow precipitate was collected, centrifuged, washed three times with water, and dried at 65 °C in vacuum overnight. A series of NiO/TiO_2 composites containing 0, 0.05, 0.2, 0.5, and 1 wt % of nickel were produced by only adding different amount of nickel powder.

2.3. Instruments. Powder X-ray diffraction (XRD) patterns were obtained to certify the phase composition of the materials on a Bruker D8-Discover with Cu-Kα irradiation (λ = 0.1542 nm). X-ray photoelectron spectroscopy (XPS) was used over a 2000 XPS system equipped with Al Kα source and calibrated according to the C 1s signal at 284.6 eV. Scanning electron microscopy (SEM, FEI INSPECT F50) was measured to determine the size and morphology of samples. High-resolution transmission electron microscopy (HRTEM) and transmission electron microscope (TEM) images were performed on FEI Tecnai G2 F20 and Hitachi H600. Using UV-visible diffuse reflectance spectra (UV-vis DRS, Shimadzu UV-3600), the absorption spectra of the samples were acquired. The Brunauer-Emmett-Teller (BET) was determined by a Mieromerities ASAP 2010 BET instrument using liquid nitrogen. Temperature-programmed desorption (TPD) was carried out on an AutoChem II 2920 chemical adsorption instrument.

2.4. Photocatalytic activity measurements. Photocatalytic reduction of CO_2 with H_2O was conducted in a quartz glass reactor with an inner volume of 100 mL (see Figure S1 for the test

system). The AMF generator consists of a rectifier and an inverter with 100 kHz and an intensity of 50 mT. Firstly, the catalyst (0.1 g) was uniformly dispersed in 0.4 g of quartz wool and set into the middle of the quartz reactor. Secondly, the reactor was purged with nitrogen for 30 min and then filled with CO_2 and 1 mL of H_2O. Finally, after adding the reactants, the reactor was placed in a 6 cm diameter copper coil with cooling water and illuminated with simulated sunlight (300 W Xe lamp). Gas in the reactor was sampled every 0.5 h and detected by a gas chromatography (GC-9860-5C).

2.5. Photoelectrochemical tests. Photoelectrochemical measurements were performed on a CHI660E electrochemical workstation (Chenhua Instrument) with a standard three-electrode system in a 0.1 M Na_2SO_4 aqueous solution. A saturated calomel electrode (SCE) and a Pt electrode were used as the reference and counter electrodes, respectively. 5 mg of the sample was uniformly dispersed in 1 mL of ethanol. 20 μL of Nafion was then added to the mixture which was subsequently shaked well. The different kinds of suspensions (100 μL) were prepared on a fluorine-doped tin oxide (FTO) glass as working electrodes with the working area of 1 cm^2. The I-t curves were recorded under the illumination of the Xe lamp with a bias potential of 0.1 V vs. SCE electrode and light ON-OFF intervals of 20 s. Electrochemical impedance spectroscopy (EIS) was measured to investigate the charge transfer process at the semiconductor with the frequency from 10^5 Hz to 10^{-1} Hz. Linear sweeping voltammogram (LSV) curves were performed with or without the AMF (~50 mT) at a scan rate of 5 mV/s to look into the interaction between the AMF and the photogenerated electron. Mott-Schottky measurements were obtained by coupling AMF or with no alternating magnetic field (NAMF), in the presence

of light illumination or not, to understand the flat-band potentials of the catalysts and calculate the concentration of charge carriers.

3. RESULTS AND DISCUSSION

Figure 1a shows the XRD patterns of the catalysts. Obviously, the NiO/TiO_2 samples have the same diffraction peaks as that of P25, indicating that the crystal phase and composition were well maintained after the hydrothermal process. All the peaks are well indexed to the anatase and rutile phases (JCPDS No. 21-1272 and JCPDS No. 21-1276, tetragonal). Additionally, the Ni-related peaks can not be detected, which could be attributed to the high dispersion of Ni species and low loading amount. The main reasons may be either the content of Ni is too low to reach detecting limit or Ni is localized on the surface of TiO_2. This result suggests that the crystalline structure of the NiO/TiO_2 catalysts remains virtually unchanged with the addition of Ni species.

The surface chemical environment and electronic structure of the catalysts were investigated by XPS.[23] As shown in Figure 1b, the XPS survey pattern of the 0.1% NiO/TiO_2 catalyst, while C, Ti, and O elements are obvious, there is no prominent peak represented to Ni, indicating the relatively low Ni content at the surface. All the binding energy values were calibrated by the C 1s located at 284.60 eV, as shown in Figure 1c. The high-resolution scans of Ti 2p and O 1s demonstrate that they are in their typical chemical states in TiO_2, as shown in Figure 1, d and e. Two O 1s peaks at 531.68 and 533.08 eV correspond to the surface hydroxyl oxygen and oxygen atoms from water molecules.[24-25] To understand the state of Ni species, high-resolution scans over 0.1% NiO/TiO_2 and 1% NiO/TiO_2 catalysts were carried out for comparison, as shown in Figure 1f. Different from 0.1% NiO/TiO_2 with no signals, 1% NiO/TiO_2 presents two notable

peaks at 855.41 and 873.38 eV, which are the typical binding energies of Ni $2p_{3/2}$ and Ni $2p_{1/2}$ in NiO, with two satellite peaks 861.67 and 880.90 eV, respectively.[23, 26]

The surface topography and composition of TiO_2 (P25) and 0.1% NiO/TiO_2 catalysts were characterized by SEM, as shown in Figure 2, a and b. The addition of Ni does not affect the original morphology of TiO_2 too much. The as-prepared catalysts consist of agglomerated particles. No clear evidence for the presence of NiO particles can be found, which agrees well with the result of the BET (see Figure S2) and XRD patterns (see Figure 1a). Table S1 summarizes the surface area and the characteristics of the pores of the catalysts. The BET analysis and the Barrett-Joyner-Halenda (BJH) method indicate that the surface areas are 48.58 and 56.79 m^2/g, with the pore size distribution of 22.82 and 17.52 nm for the TiO_2 and 0.1% NiO/TiO_2, respectively. To clarify the state of Ni species, TEM characterization was conducted, as shown in Figure 2, c-g. As shown in Figure 2c, it is speculated that the small solid particle with a strong contrast in the middle of the image might be a NiO particle.[27] By the way, the size of the catalyst particles was about 20 nm. The well-defined lattice fringes in HRTEM images indicates that the catalyst is in good crystallinity, as shown in Figure 2, d-g. The lattice fringes with space distances of 0.32 nm, 0.35 nm, and 0.24 nm (see Figure 2e, Figure 2f, and Figure 2g related to the yellow, red, and green areas in Figure 2d) correspond to the (110) plane of rutile TiO_2, (101) plane of anatase TiO_2, and (111) plane of NiO, respectively. The distribution of the elements in 0.1% NiO/TiO_2 catalyst was determined by STEM and energy dispersive X-ray spectroscopy (EDS), as shown in Figure 2, h-l. All elements, including Ni, Ti, and O, are demonstrated homogeneously distributed throughout the catalyst particles.

The transient photocurrent responses of TiO_2 (P25) and the NiO/TiO_2 catalysts were performed to analyze the separation efficiency of photogenerated carriers upon cycled on-off light illumination, as shown in Figure 3a.[28] The interval of each on-off cycle is 20 s. Under open circuit potential (OCP), the current density of all samples was zero without light irradiation. The 0.1% NiO/TiO_2 catalyst showed the highest current density value up to 3.5 $\mu A \cdot cm^{-2}$ upon light irradiation. The higher photoresponse current corresponds to better photoactivity. The slight decline in current density after an on-off switch loop could be due to the cracks and loss of the catalyst film on the FTO.[29] The comparison of electrochemical impedance spectra (EIS), which was performed to explore the charge transport dynamics of the samples, was showed in Figure 3b. The EIS was measured under OCP in a frequency range of 0.1-10000 Hz. The diameters of the semicircles of the photocatalysts were obtained in the Nyquist plots. The 0.1% NiO/TiO_2 catalyst displayed a minimum semicircular diameter which implies faster charge transfer and restricted electron-hole recombination. Moreover, according to the I-t curve and EIS analysis, the 0.1% NiO/TiO_2 catalyst is expected to have the best photocatalytic CO_2 reduction activity among all the as-prepared catalysts. The speculation is validated by the photocatalytic results. As shown in Figure 4a, TiO_2 (P25) and a series of NiO/TiO_2 catalysts were employed for photocatalytic CO_2 reduction in the presence of water vapor. The 0.1% NiO/TiO_2 catalyst showed the highest CH_4 yield, which is up to 21.51 μmol/g, after three hours of simulated sunlight irradiation. The highest CO yield was obtained over the 0.2% NiO/TiO_2 sample, reaching 13.80 μmol/g. The CO and CH_4 yields of other catalysts were summarized in Table S3. It is obvious that the 0.1% NiO/

TiO_2 catalyst showed best performance toward C-element conversions and CH_4 production. We then took it as the model photocatalyst to investigate the effect of the AMF.

The linear sweep voltammetry (LSV) of 0.1% NiO/TiO_2 catalyst was performed under the AMF and NAMF conditions and with or without light illumination, as shown in Figure 3c. The *iR* correction was applied to the original data to eliminate the effect of ohmic resistance on the intrinsic behavior of the catalyst.[30] The onset potentials of the LSV curves were almost identical in the dark regardless of AMF or NAMF. Similar results were found in the presence of light irradiation. By comparing the data under the condition of NAMF with dark and NAMF with light, the onset potentials tested with light showed more positive compared to in the dark, which was nearly consistent with the data tested under the condition of AMF with dark and AMF with light. It is clear that light irradiation can significantly reduce the reaction barrier, whereas AMF has little effect on the reaction barrier.[31] However, it is found that without light irradiation the current density was increased by 12.10 $\mu A \cdot cm^{-2}$ at 0.3 V *vs*. RHE by integrating AMF. This phenomenon indicates that AMF could promote the charge separation on the catalyst surface.[32] Under the condition of NAMF, the current density was increased by 18.10 $\mu A \cdot cm^{-2}$ at 0.3 V *vs*. RHE upon light irradiation, indicating the good photoresponse ability of the catalyst.[33] With light illumination and applying AMF, the current density could be increased by as high as 29.09 $\mu A \cdot cm^{-2}$ at 0.3 V *vs*. RHE. It is believed that charge separation could be significantly promoted by integrating AMF into the light illumination process.

The flat potential and the charge carrier concentration of the 0.1% NiO/TiO_2 catalyst were analyzed by the Mott-Schottky plos obtained at 100 Hz under AMF and NAMF conditions and

with or without light illumination, as shown in Figure 3d. The positive slope of the M-S plots indicate the n-type behavior of the samples. The value of the flat band potential E_{fb} and the carriers concentration could be calculated using the M-S equation (*Eq. 1*):[34]

$$\frac{1}{C^2}=\left[\frac{2}{\varepsilon\varepsilon_0 eN A^2}\right]\left[E-E_{fb}-\frac{k_B T}{e}\right] \quad (1)$$

Where C is the differential capacitance, ε is the dielectric constant of the semiconductor, ε_0 is the permittivity of free space, e is the electric charge, N is the density of carriers, A is the area of the sample in solution, E is the applied potential, E_{fb} is the flat band potential, k_B is the Boltzmann constant, and T is the absolute temperature. Since the value of $\frac{k_B T}{e}$ is only ~25 mV at room temperature, the flat band potential E_{fb} can be determined by extrapolating the M-S slope to $\frac{1}{C^2}=0$.[35] When the Mott–Schottky plot becomes linear, N is obtained by the equation slope = $\frac{2}{\varepsilon\varepsilon_0 e N_D A^2}$. The value of the dielectric constant of TiO_2 varies from 86 to 173, so we set the dielectric constant of TiO_2 at 100 to estimate carrier density N.[36] The obtained values of E_{fb} and N tested under different conditions was presented in Table 1. Under the NAMF condition, the E_{fb} shifted positively by 0.1 V with the light illumination compared to the dark. This is attributed to the generation of the photovoltage of the catalyst in the FTO.[37] The intercept of the M-S plot on the x-axis was almost unchanged under the AMF and NAMF conditions without light irradiation.

The reason could be attributed to that integration of AMF did not generate additional voltage in the catalyst to change the position of E_{fb}. With light illumination, the E_{fb} shifted positively by 0.08 V in the presence of AMF compared to that of NAMF condition. It demonstrates that the AMF can significantly enhance the photovoltage upon light irradiation. In this case, recombination of photogenerated carriers can be effectively suppressed by magnetic field. These conclusions are generally consistent with the analysis of the data on carrier density, as shown in Table 1. Under NAMF condition, the calculated carrier density (N) was increased by 2.50×10^{24} cm^{-3} with light illumination compared to that of dark. This is due to the higher carrier density resulting from light excitation. The slope under the NAMF was smaller than under the AMF with the dark condition, which probably caused the AMF to enhance the surface potential of the catalyst, accelerating the electron transport rate.[32] With light illumination, the N was increased by 4.53×10^{24} cm^{-3} under the AMF compared to the NAMF condition. In the presence of light, AMF enables an increment of 70% for charge density, in which the AMF could significantly promote the separation of photogenerated charges and inhibit their recombination.

The effects AMF for photocatalytic CO_2 reduction with H_2O vapor over 0.1% NiO/TiO_2 catalyst were investigated. The results were displayed in Figure 4, b-d. The yields of CO and CH_4 under different conditions were summarized in Table S4. Without simulated sunlight irradiation, there were no CH_4 and negligible CO products (due to scattered sunlight in the environment). The yield of CO reached to 7.99 μmol g^{-1} under the NAMF with light, which yet was almost unchanged after applying AMF. However, the yield of CH_4 showed a remarkable increase from 21.51 μmol g^{-1} to 67.32 μmol g^{-1} by integrating AMF, as shown in Figure 4b.

Taken together, we can conclude that without light irradiation, integration of AMF has little influence on the reaction. However, the effect of AMF can expressed under simulated sunlight irradiation, by which CO_2-to-CH_4 conversion could be significantly enhanced. All these results including photocatalytic tests, LSV curves, and the Mott-Schottky plots demonstrate that the AMF can significantly enhance the separation of the photogenerated electron-hole pairs and suppress the recombination as well to promote the conversion of CO_2.

Figure 4, c and d depict the time dependence of photocatalytic production of CO and CH_4. The concentrations of CO and CH_4 gradually reached reaction equilibrium in 3 hours of simulated sunlight irradiation. The AMF had no apparent effect on CO_2-to-CO conversion throughout the reaction process. The yield of CH_4 was 0 μmol g^{-1} without the light and dramatically enhanced upon simulated sunlight irradiation. The CO_2-to-CH_4 conversion in the presence of light reached close to equilibrium in a shorter time under the AMF compared to NAMF. It indicates the positive role of AMF for remarkably increasing the conversion rate from CO_2 to CH_4. The catalytic performance over TiO_2 (P25), 0.05% NiO/TiO_2, 0.2% NiO/TiO_2, 0.5% NiO/TiO_2, and 1% NiO/TiO_2 catalysts under the AMF and NAMF conditions and with or without light illumination was also investigated as shown in Figure S6 and the yields of different products were summarized in Table S5. These samples showed almost identical catalytic trends to that of 0.1% NiO/TiO_2 catalyst.

The TiO_2 (P25) and NiO/TiO_2 catalysts were further analyzed by the UV-vis absorption spectra, as shown in Figure S3a. All the prepared catalysts presented an absorbance edge lower than 450 nm, yet 1% NiO/TiO_2 catalyst showed a notable absorption from 400 to 800 nm. The

Tauc plot was calculated to estimate the band-gap energy (E_g) of the catalysts according to the following formula (*Eq. 2*):

$$(\alpha h\upsilon)^{1/r} = A(h\upsilon - E_g) \qquad (2)$$

Typically, where $h\upsilon$ is the energy of light and α is the absorption coefficient of the material. For the TiO_2 substrate, which is an indirect allowed transitions semiconductor, the value of the exponent r is 2.[38] The band-gap energies of TiO_2 (P25) and NiO/TiO_2 catalysts were presented in Table S2. The biggest E_g of 2.77 eV was obtained at 0.1% Ni addition. The narrower the E_g indicates a broader interval of catalyst response to light. The valence band spectra were measured to investigate the valence band maximum (VBM) position, as shown in Figure S3b. The VBM of the samples shifted positively when the content of Ni is less than 0.1%, beyond which, the VBM shifted negatively. This may relate to the combination of oxygen vacancies caused by Ni-doping and NiO on the substrate catalyst surface.[39-40] It is well known that the E_{fb} of many n-type semiconductors is 0.1-0.3 eV more positive than the CBM.[41] The conduction band minimum (CBM) was calculated to be -0.01 eV by a combination of the band-gap energy and the VBM. On the other hand, the E_{fb} was 0.25 eV *vs*. RHE measured by Mott-Schottky plot. The 0.1% NiO/TiO_2 catalyst has a more positive valence band at 2.77 eV indicating stronger oxidation performance.[42]

The CO_2-TPD was conducted to evaluate the CO_2 adsorption active sites, as shown in Figure S5. The modes of CO_2 adsorption were reported to be mainly in the forms of CO_2 molecules adsorption and carbonate.[43] The peaks observed in profiles were molecularly adsorbed CO_2,

bicarbonate (HCO_3^-), and bidentate carbonates (b-CO_3^{2-}), respectively.[43-44] There were no significant changes in the desorption peak centered at 90 °C for the two catalysts, indicating that Ni species did not affect the CO_2 molecules adsorption (75-180 °C). The desorption peak centered at 240 °C was attributed to the generation of HCO_3^- (180-380 °C), which might result in the reaction of CO_2 and the surface hydroxyls. More surface hydroxyls observed in NiO/TiO_2 are mainly due to the O-vacancy formed by Ni doping.[40, 45] The result is the same as that presents in Figure S4, indicating that the O 1s peaks of the surface hydroxyl group (~531.68 eV) and surface water (~533.08 eV) were significantly enhanced on the 0.1% NiO/TiO_2 catalyst compared to TiO_2 (P25). The desorption capacity of 0.1% NiO/TiO_2 catalyst at 240 °C was generally improved compared to TiO_2 (P25), which could be attributed to the surface hydroxyls absorption enhanced by Ni species. The b-CO_3^{2-} (380–550 °C) was appeared at approximately 380 °C and 395 °C for TiO_2 (P25) and 0.1% NiO/TiO_2, respectively. The desorption peak of 0.1% NiO/TiO_2 catalyst was more considerable than that of TiO_2 (P25), and the desorption temperature was increased by 15 °C at the same time. This enhancement is contributed by the surface NiO, which increases the binding between CO_2 and the catalyst and benefits to CO_2 hydrogenation.[46] Another peak centered at 475 °C also belonged to b-CO_3^{2-}, which might due to the interaction of CO_2 and TiO_2 on the surface of the catalyst.

We finally tried to further demonstrate the role of AMF by in-depth analyze the photocatalytic mechanism over the 0.1% NiO/TiO_2 catalyst. There are three critical factors in photocatalytic CO_2 reduction: (1) the light-harvesting efficiency, (2) the adsorption/activation properties for reactants, and (3) the separation and transfer of photogenerated electron-hole pair. The 0.1%

NiO/TiO_2 catalyst has the smallest E_g indicating the most efficient light-harvesting. The BET analysis and the BJH method demonstrate the mesoporous nature and the large surface area of the catalyst, which facilitates the adsorption of the reactants. The CO_2-TPD results clarified that the CO_2 adsorption active sites were enhanced by Ni doping and the surface NiO. The EIS results indicated the separation and transfer of the photoexcited charge were improved via the addition of 0.1% Ni. The Mott-Schottky plots suggest that the AMF increased the concentration of the carriers and improved the oxidation performance of the catalyst as well.

Based on the above experimental results, we deduced the possible mechanism for photocatalytic CO_2 reduction to CH_4, as shown in Figure 5. The photogenerated electron-hole pairs are generated on the TiO_2 semiconductor under the simulate sunlight irradiation—the holes on the TiO_2 valence band oxide the adsorbed H_2O molecules to form H^+ and ·OH radicals[47]. Next, the adsorbed H_2O can react with the ·OH radicals to produce H^+ and O_2. Simultaneously, the electrons are excited to the conduction band of TiO_2 and then transfer to the NiO particle on the TiO_2 substrate. The absorbed CO_2 molecules on the NiO particle can be reduced by electrons and combined with H^+ to produce CH_4. Finally, the stability of the 0.1% NiO/TiO_2 catalyst was evaluated, as shown in Figure S7. The yields of CH_4 were no significant decline after five-time cycled tests.

4. CONCLUSIONS

In summary, we demonstrate significant effect of AMF on enhancing photocatalytic CO_2-to-CH_4 conversion over NiO/TiO_2 catalysts. The yields of CH_4 improve by approximately 213% by integrating AMF into the photocatalytic system. The enhancement should be due to enhancement

of the oxidation over the catalysts induced by AMF, which is more favorable to the generation of hydroxyl radicals and oxygen. The enhanced productivity of CH_4 also attributes to the accelerated photogenerated charge transfer while inhibited recombination in the presence of AMF. The Ni species act as the adsorption/activation sites of CO_2 to promote the reduction of CO_2 by photogenerated electrons, and at the same time, facilitate the formation of surface hydroxyl groups to improve the oxidation of water by holes. By coupling the AMF to the photocatalytic reaction, the concentration of the photogenerated carriers is significantly increased. This work provides an original scheme for photocatalytic CO_2-to-CH_4 conversion in H_2O vapor, and the coupled optical-magnetic system can also be applied to other photocatalytic reaction systems.

ASSOCIATED CONTENT

Supporting Information

BET results; energy band position; yield of the CO and CH_4 from different catalysts; yield of the CO and CH_4 from 0.1% NiO/TiO_2 catalyst with different conditions; yield of the CO and CH_4 from different catalysts with various conditions; schematic diagram; BET and BJH methods; UV-vis absorption spectra and XPS valence band spectra; contrast XPS of TiO_2 (P25) and 0.1% Ni/TiO_2 catalys; CO_2-TPD profiles; yield plot; and recycling studies.

AUTHOR INFORMATION

Corresponding Authors

*E-mail for N. L.: naixuli@seu.edu.cn

*E-mail for D. J.: dwjing@mail.xjtu.edu.cn

ORCID

Naixu Li: 0000-0002-0524-5475

Dengwei Jing: 0000-0001-6062-9239

Notes

The authors declare no competing financial interest.

ACKNOWLEDGMENTS

This work was financially supported by the National Natural Science Foundation of China (No. 22078057, No. 51876173), Fok Ying-Tung Education Foundation (No. 171048), the Natural Science Foundation of Jiangsu Province (No. BK20190054), Fundamental Research Funds for the Central Universities of China (No. 3207045403, 3207045409, 3207046414), Foundation of Jiangsu Key Laboratory for Biomass Energy and Material (JSBEM202001), Priority Academic Program Development of Jiangsu Higher Education Institutions (PAPD) and Zhongying Young Scholars of Southeast University.

REFERENCES

(1) Matavos-Aramyan, S.; Soukhakian, S.; Jazebizadeh, M. H.; Moussavi, M.; Hojjati, M. R., On engineering strategies for photoselective CO_2 reduction – A thorough review. *Appl. Mater. Today* **2020;** 18: 100499.

(2) Zheng, Y.; Zhang, W.; Li, Y.; Chen, J.; Yu, B.; Wang, J.; Zhang, L.; Zhang, J., Energy related CO_2 conversion and utilization: Advanced materials/nanomaterials, reaction mechanisms and technologies. *Nano Energy* **2017;** 40: 512-539.

(3) Habisreutinger, S. N.; Schmidt-Mende, L.; Stolarczyk, J. K., Photocatalytic reduction of CO_2 on TiO_2 and other semiconductors. *Angew. Chem. Int. Ed.* **2013;** 52: 7372-7408.

(4) Zhao, G.; Huang, X.; Wang, X.; Wang, X., Progress in catalyst exploration for heterogeneous CO_2 reduction and utilization: a critical review. *J. Mater. Chem. A* **2017;** 5: 21625-21649.

(5) Din, I. U.; Shaharun, M. S.; Alotaibi, M. A.; Alharthi, A. I.; Naeem, A., Recent developments on heterogeneous catalytic CO_2 reduction to methanol. *J. CO2 Util.* **2019;** 34: 20-33.

(6) Low, J.; Yu, J.; Jaroniec, M.; Wageh, S.; Al-Ghamdi, A. A., Heterojunction photocatalysts. *Adv. Mater.* **2017;** 29: 1601694.

(7) Shehzad, N.; Tahir, M.; Johari, K.; Murugesan, T.; Hussain, M., A critical review on TiO_2 based photocatalytic CO_2 reduction system: Strategies to improve efficiency. *J. CO2 Util.* **2018;** 26: 98-122.

(8) Fujishima, A.; Honda, K., Electrochemical photolysis of water at a semiconductor electrode. *Nature* **1972;** 238: 37-38.

(9) Inoue, T.; Fujishima, A.; Konishi, S.; Honda, K., Photoelectrocatalytic reduction of carbon dioxide in aqueous suspensions of semiconductor powders. *Nature* **1979;** 277: 637-638.

(10) Xu, H.-Q.; Hu, J.; Wang, D.; Li, Z.; Zhang, Q.; Luo, Y.; Yu, S.-H.; Jiang, H.-L., Visible-light photoreduction of CO_2 in a metal-organic framework: Boosting electron-hole separation via electron trap states. *J. Am. Chem. Soc.* **2015;** 137: 13440-13443.

(11) Isari, A. A.; Hayati, F.; Kakavandi, B.; Rostami, M.; Motevassel, M.; Dehghanifard, E., N, Cu co-doped TiO_2@functionalized SWCNT photocatalyst coupled with ultrasound and visible-light: An effective sono-photocatalysis process for pharmaceutical wastewaters treatment. *Chem. Eng. J.* **2020;** 392: 123685.

(12) Chueh, W. C.; Falter, C.; Abbott, M.; Scipio, D.; Furler, P.; Haile, S. M.; Steinfeld, A., High-flux solar-driven thermochemical dissociation of CO_2 and H_2O using nonstoichiometric ceria. *Science* **2010;** 330: 1797-1801.

(13) Xie, T.; Liu, C.; Xu, L.; Yang, J.; Zhou, W., Novel heterojunction $Bi_2O_3/SrFe_{12}O_{19}$ magnetic photocatalyst with highly enhanced photocatalytic activity. *J. Phys. Chem. C* **2013;** 117: 24601-24610.

(14) Li, J.; Pei, Q.; Wang, R.; Zhou, Y.; Zhang, Z.; Cao, Q.; Wang, D.; Mi, W.; Du, Y., Enhanced photocatalytic performance through magnetic field boosting carrier transport. *ACS Nano* **2018;** 12: 3351-3359.

(15) Garcés-Pineda, F. A.; Blasco-Ahicart, M.; Nieto-Castro, D.; López, N.; Galán-Mascarós, J. R., Direct magnetic enhancement of electrocatalytic water oxidation in alkaline media. *Nat. Energy* **2019;** 4: 519-525.

(16) Li, R.; Yang, Y.; Li, R.; Chen, Q., Experimental and theoretical studies on the effects of magnetic fields on the arrangement of surface spins and the catalytic activity of Pd nanoparticles. *ACS Appl. Mater. Interfaces* **2015;** 7: 6019-6024.

(17) Xie, T.; Xu, L.; Liu, C.; Yang, J.; Wang, M., Magnetic composite BiOCl-$SrFe_{12}O_{19}$: a novel p-n type heterojunction with enhanced photocatalytic activity. *Dalton Trans.* **2014;** 43: 2211-2220.

(18) Welle, A.; Staerk, H.; Treichel, R., Magnetic-field effects on geminate radical-pair recombination. *Faraday Discuss. Chem. Soc.* **1984;** 78: 271-278.

(19) Gracia, J., Spin dependent interactions catalyse the oxygen electrochemistry. *Phys.Chem.Chem.Phys.* **2017;** 19: 20451-20456.

(20) Fay, T. P.; Manolopoulos, D. E., Radical pair intersystem crossing: Quantum dynamics or incoherent kinetics? *J. Chem. Phys.* **2019;** 150: 151102.

(21) Ivanov, K. L.; Wagenpfahl, A.; Deibel, C.; Matysik, J., Spin-chemistry concepts for spintronics scientists. *Beilstein J. Nanotechnol.* **2017;** 8: 1427-1445.

(22) Pan, H.; Jiang, X.; Wang, X.; Wang, Q.; Wang, M.; Shen, Y., Effective magnetic field regulation of the radical pair spin states in electrocatalytic CO_2 reduction. *J. Phys. Chem. Lett.* **2020;** 11: 48-53.

(23) Peck, M. A.; Langell, M. A., Comparison of nanoscaled and bulk NiO structural and environmental characteristics by XRD, XAFS, and XPS. *Chem. Mater.* **2012;** 24: 4483-4490.

(24) Wang, S.; Chen, P.; Bai, Y.; Yun, J.-H.; Liu, G.; Wang, L., New $BiVO_4$ dual photoanodes with enriched oxygen vacancies for efficient solar-driven water splitting. *Adv. Mater.* **2018;** 30: 1800486.

(25) Cheng, J.; Liu, P.; Peng, T.; Liu, Q.; Chen, W.; Liu, B.; Yuan, Y.; Zhang, W.; Song, F.; Gu, J.; Zhang, D., Mechanically alloyed $NiTiO_3$/transition metal heterostructures: introducing oxygen vacancies for exceptionally enhanced hydrogen evolution reaction activity. *J. Mater. Chem. A* **2020;** 8: 14908-14914.

(26) Yu, J.; Hai, Y.; Cheng, B., Enhanced photocatalytic H_2-production activity of TiO_2 by $Ni(OH)_2$ cluster modification. *J. Phys. Chem. C* **2011;** 115: 4953-4958.

(27) Ciocarlan, R.-G.; Seftel, E. M.; Mertens, M.; Pui, A.; Mazaj, M.; Novak Tusar, N.; Cool, P., Novel magnetic nanocomposites containing quaternary ferrites systems $Co_{0.5}Zn_{0.25}M_{0.25}Fe_2O_4$ (M=Ni, Cu, Mn, Mg) and TiO_2-anatase phase as photocatalysts for wastewater remediation under solar light irradiation. *Mater. Sci. Eng., B* **2018;** 230: 1-7.

(28) Cong, Y.; Zhang, J.; Chen, F.; Anpo, M.; He, D., Preparation, photocatalytic activity, and mechanism of nano-TiO_2 co-doped with nitrogen and iron (III). *J. Phys. Chem. C* **2007;** 111: 10618-10623.

(29) Yang, P.; Zhuzhang, H.; Wang, R.; Lin, W.; Wang, X., Carbon vacancies in a melon polymeric matrix promote photocatalytic carbon dioxide conversion. *Angew. Chem.* **2019;** 58: 1134-1137.

(30) Xie, L.; Zhang, R.; Cui, L.; Liu, D.; Hao, S.; Ma, Y.; Du, G.; Asiri, A. M.; Sun, X., High-performance electrolytic oxygen evolution in neutral media catalyzed by a cobalt phosphate nanoarray. *Angew. Chem. Int. Ed.* **2017;** 56: 1064-1068.

(31) Lan, Y.; Xie, Y.; Chen, J.; Hu, Z.; Cui, D., Selective photocatalytic CO_2 reduction on copper-titanium dioxide: a study of the relationship between CO production and H_2 suppression. *Chem. Commun.* **2019;** 55: 8068-8071.

(32) Gao, W.; Liu, Q.; Zhang, S.; Yang, Y.; Zhang, X.; Zhao, H.; Qin, W.; Zhou, W.; Wang, X.; Liu, H.; Sang, Y., Electromagnetic induction derived micro-electric potential in metal-semiconductor core-shell hybrid nanostructure enhancing charge separation for high performance photocatalysis. *Nano Energy* **2020**; 104624.

(33) Han, H.-X.; Shi, C.; Zhang, N.; Yuan, L.; Sheng, G.-P., Visible-light-enhanced Cr(VI) reduction at Pd-decorated silicon nanowire photocathode in photoelectrocatalytic microbial fuel cell. *Sci. Total Environ.* **2018;** 639: 1512-1519.

(34) De Gryse, R.; Gomes, W. P.; Cardon, F.; Vennik, J., on the interpretation of Mott–Schottky plots determined at semiconductor/electrolyte systems. *J. Electrochem. Soc.* **2019;** 122: 711-712.

(35) Kunadian, I.; Lipka, S. M.; Swartz, C. R.; Qian, D.; Andrews, R., Determination of carrier densities of boron- and nitrogen-doped multiwalled carbon nanotubes using Mott–Schottky plots. *J. Electrochem. Soc.* **2009;** 156: K110-K115.

(36) Harrington, S. P.; Devine, T. M., Analysis of electrodes displaying frequency dispersion in Mott-Schottky tests. *J. Electrochem. Soc.* **2008;** 155: C381-C386.

(37) Patel, M.; Kumar, M. K.; Kim, J.; Kim, Y. K., Photocurrent enhancement by a rapid thermal treatment of nanodisk-shaped SnS photocathodes. *J. Phys. Chem. Lett.* **2017;** 8: 6099-6105.

(38) Suram, S. K.; Newhouse, P. F.; Gregoire, J. M., High throughput light absorber discovery, Part 1: an algorithm for automated Tauc analysis. *ACS Comb. Sci.* **2016;** 18: 673-681.

(39) Hossain, F. M.; Murch, G. E.; Sheppard, L.; Nowotny, J., *Ab initio* electronic structure calculation of oxygen vacancies in rutile titanium dioxide. *Solid State Ion* **2007;** 178: 319-325.

(40) Sun, C.; Liao, T.; Lu, G. Q.; Smith, S. C., The role of atomic vacancy on water dissociation over titanium dioxide nanosheet: A density functional theory study. *J. Phys. Chem. C* **2012;** 116: 2477-2482.

(41) Chun, W.-J.; Ishikawa, A.; Fujisawa, H.; Takata, T.; Kondo, J. N.; Hara, M.; Kawai, M.; Matsumoto, Y.; Domen, K., Conduction and valence band positions of Ta_2O_5, TaON, and $Ta_3N_5$by ups and electrochemical methods. *J. Phys. Chem. B* **2003;** 107: 1798-1803.

(42) Zhou, Y.; Zhang, X.; Zhang, Q.; Dong, F.; Wang, F.; Xiong, Z., Role of graphene on the band structure and interfacial interaction of Bi_2WO_6/graphene composites with enhanced photocatalytic oxidation of NO. *J. Mater. Chem. A* **2014;** 2: 16623-16631.

(43) Zhao, J.; Wang, Y.; Li, Y.; Yue, X.; Wang, C., Phase-dependent enhancement for CO_2 photocatalytic reduction over CeO_2/TiO_2 catalysts. *Catal. Sci. Technol.* **2016;** 6: 7967-7975.

(44) Mao, J.; Ye, L.; Li, K.; Zhang, X.; Liu, J.; Peng, T.; Zan, L., Pt-loading reverses the photocatalytic activity order of anatase TiO_2 {001} and {010} facets for photoreduction of CO_2 to CH_4. *Appl. Catal. B* **2014;** 144: 855-862.

(45) Elahifard, M.; Heydari, H.; Behjatmanesh-Ardakani, R.; Peik, B.; Ahmadvand, S., A computational study on the effect of Ni impurity and O-vacancy on the adsorption and dissociation of water molecules on the surface of anatase (101). *J. Phys. Chem. Solids* **2020;** 136: 109176.

(46) Wang, Z.; Huang, L.; Su, B.; Xu, J.; Ding, Z.; Wang, S., Unravelling the promotional effect of La_2O_3 in Pt/La-TiO_2 catalysts for CO_2 hydrogenation. *Chem. Eur. J.* **2020;** 26: 517-523.

(47) Dilla, M.; Mateblowski, A.; Ristig, S.; Strunk, J., Photocatalytic CO_2 reduction under continuous flow high-purity conditions: Influence of light intensity and H_2O concentration. *ChemCatChem* **2017;** 9: 4345-4352.

Table 1. The flat potential E_{fb} (V) and the charge carriers density (cm^{-3}) of 0.1% NiO/TiO_2 catalyst under different conditions.

catalyst	conditions	flat potential E_{fb} (V)	carriers density (10^{24} cm^{-3})
0.1% NiO/TiO_2	NAMF dark	0.25	3.97
	AMF dark	0.24	5.68
	NAMF light	0.35	6.47
	AMF light	0.43	11.00

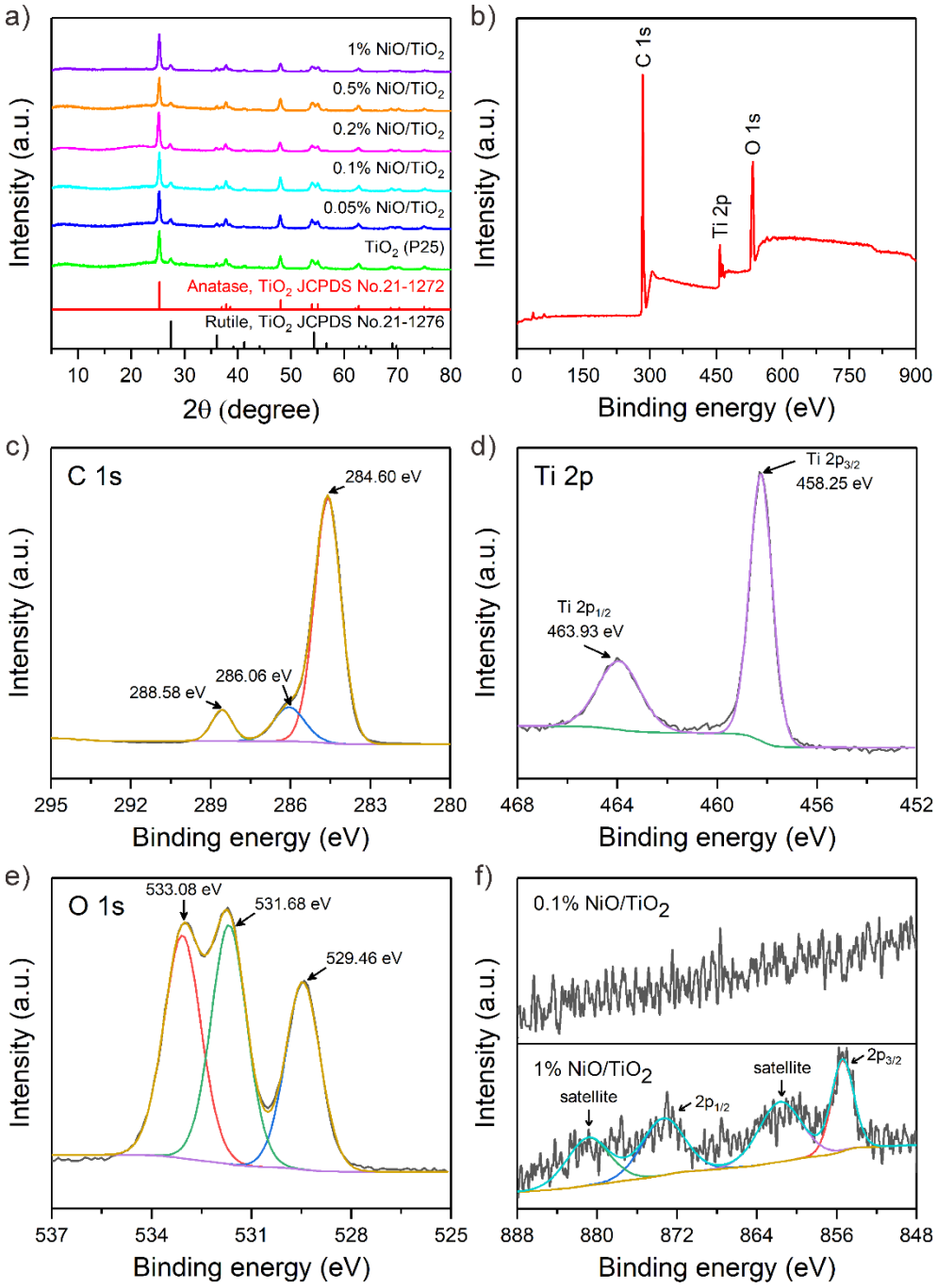

Figure 1. (a) XRD patterns of the TiO_2 (P25) and NiO/TiO_2 catalysts. (b) XPS survey spectra and (c-e) High-resolution XPS of (c) C 1s, (d) Ti 2p, and (e) O 1s spectra of the 0.1% NiO/TiO_2 catalyst. (f) High-resolution XPS spectra of Ni 2p of 0.1% NiO/TiO_2 and 1% NiO/TiO_2 catalysts.

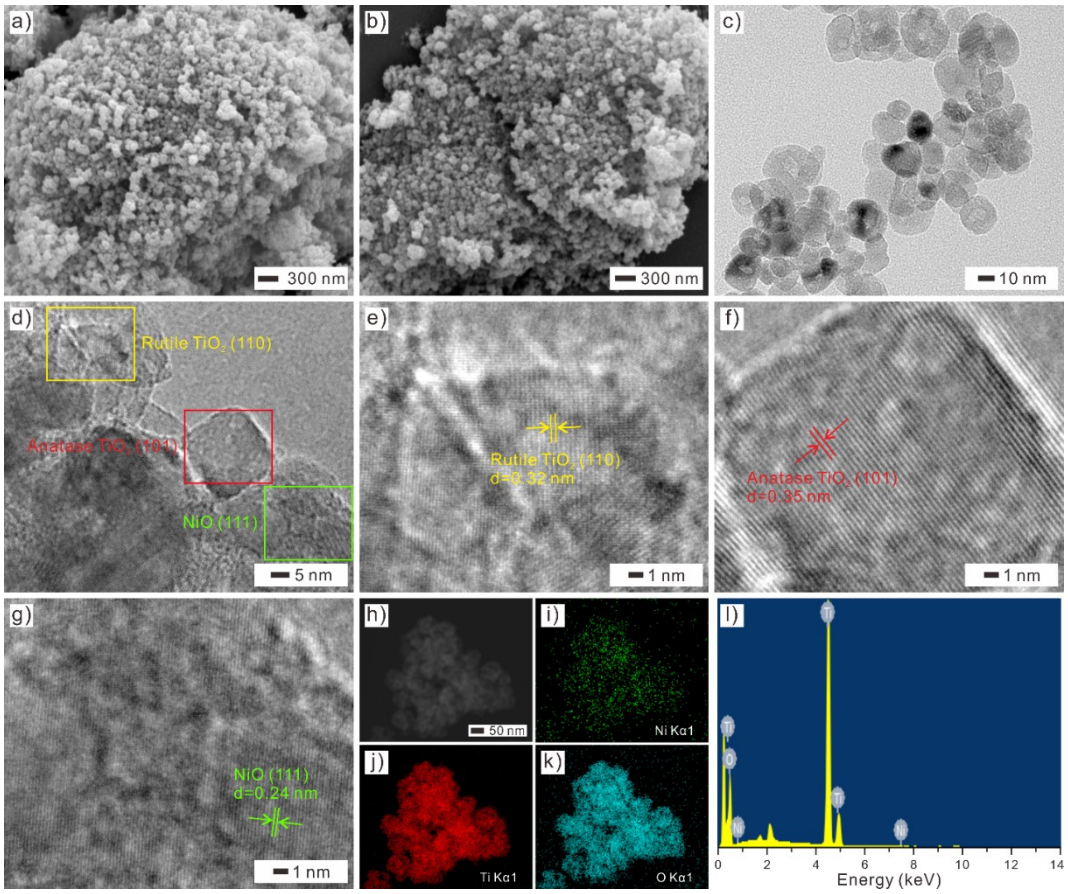

Figure 2. SEM image of (a) TiO_2 (P25), and (b) 0.1% NiO/TiO_2 catalysts. (c) TEM image, (d) HRTEM image, (e) lattice fringe of rutile TiO_2 (110), (f) lattice fringe of anatase TiO_2 (111), and (g) lattice fringe of NiO (111) of the 0.1% NiO/TiO_2 catalyst. (h) STEM image of 0.1% NiO/TiO_2 catalyst and corresponding (i-k) EDS mappings of Ni, Ti, and O, respectively. (l) EDS pattern of 0.1% NiO/TiO_2 catalyst.

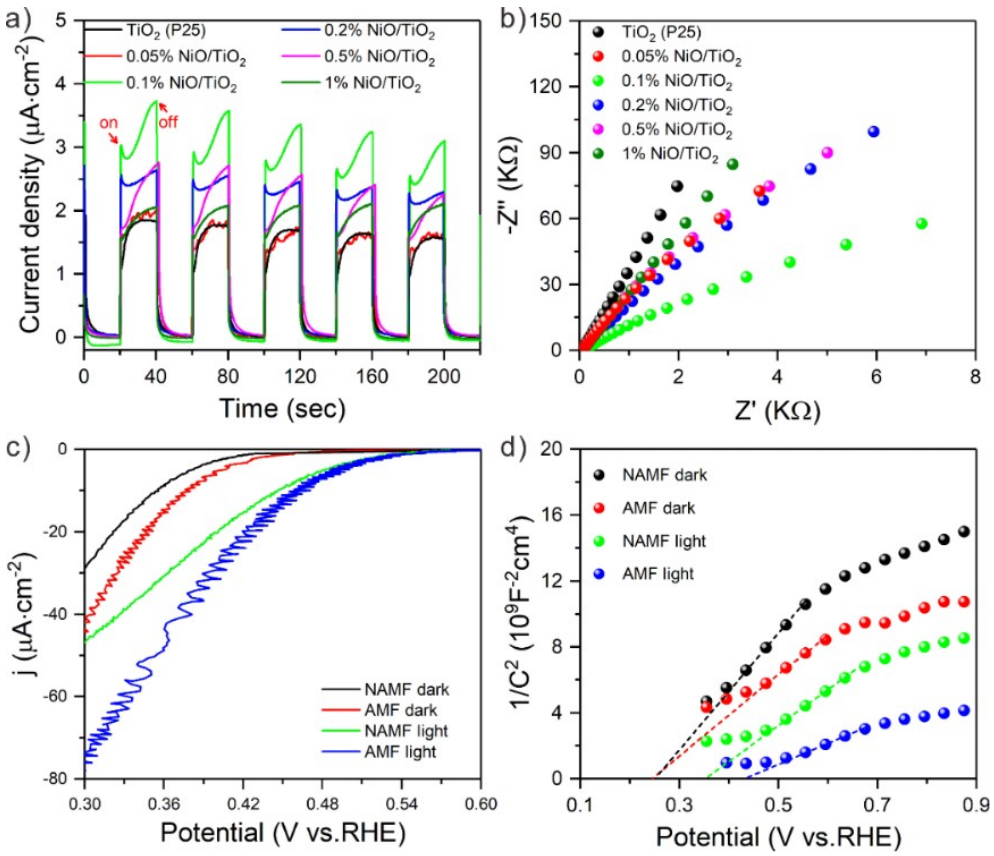

Figure 3. (a) The transient photocurrent responses, and (b) Nyquist plot of the TiO_2 (P25) and the NiO/TiO_2 catalysts. (c) linear sweep voltammograms (LSV), and (d) Mott-Schottky plots under the AMF and NAMF conditions with or without light illumination for the 0.1% NiO/TiO_2 catalyst.

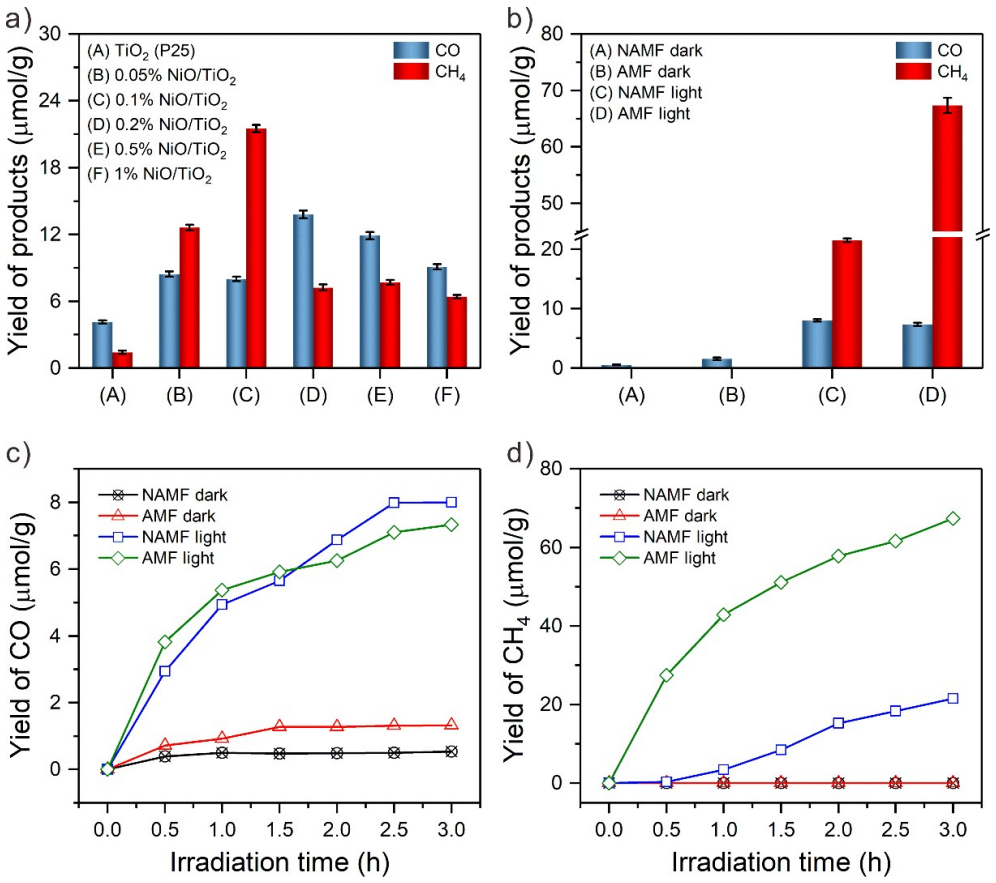

Figure 4. (a) Production of CO and CH_4 on TiO_2 (P25) and the NiO/TiO_2 catalysts for a period of 3h light illumination. (b) Production of CO and CH_4 for a period of 3h reaction under the AMF and NAMF conditions with or without light illumination. Time dependence photocatalytic production of (c) CO, and (d) CH_4 under the AMF and NAMF conditions with or without light illumination.

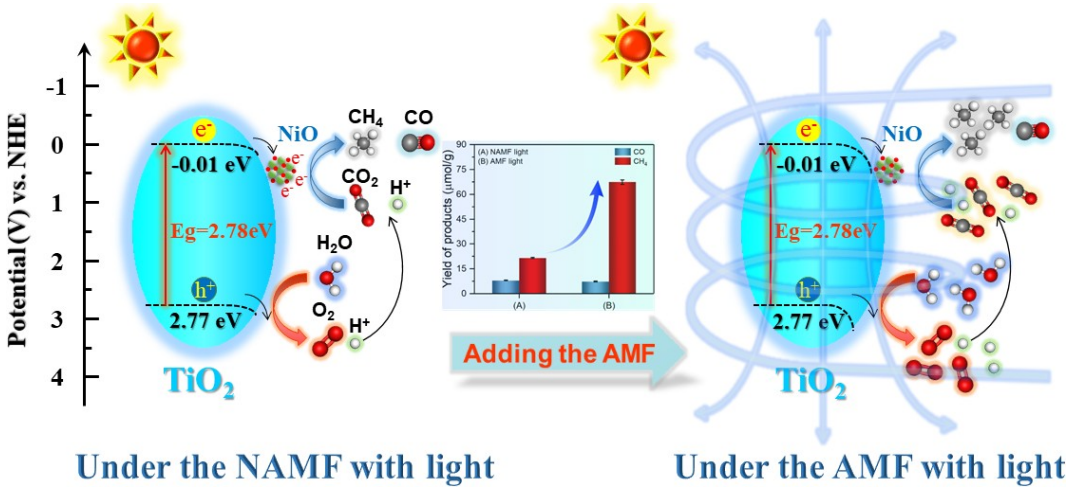

Figure 5. Schematic illustration on the mechanism involved on the surface of the 0.1% NiO/TiO_2 photocatalyst with or without the AMF.

For Table of Contents Only